Optical Tweezers and Maxwell's Demon

MARKUS ASPEGREN

DEPARTMENT OF PHYSICS
LUND UNIVERSITY

JUNE 9, 2016
PROJECT DURATION: 2 MONTHS

A thesis submitted for the degree of Bachelor of Science

Supervisors:
Prof. Jonas Johansson, LUND UNIVERSITY
Regina Schmitt, PhD Student, LUND UNIVERSITY

Contents

Abstract

Future nanoscale applications of Brownian motors will benefit from further development of stochastic thermodynamics, bridging the the properties of systems in non-equilibrium with those in equilibrium. This thesis presents the first step towards a device mimicking Maxwell's demon, which will be used for a study of systems out of equilibrium. It operates using an optical tweezer that is scanned rapidly in a line, generating an optical line trap in which a silica bead of 1 μm diffuses. The bead is confined in regions of the trap using regions of lower intensity regions as barriers, which are implemented in relation to the bead's position in the trap. Properties of these barriers are investigated by studying the diffusion of the bead following the barrier's implementation. The goal was to experimentally confirm the precise size of two generated barriers in order to find the closest distance a barrier may be implemented without affecting the bead's diffusion. The trap used proved too small to successfully do so, and instead focus was shifted towards an investigation of the intensity gradients of the barriers.

List of abbreviations

AOD   **A**cousto- **O**ptical **D**eflector
TEM   **T**ransverse **e**lectro **m**agnetic
PDSM   polydimethylsiloxane (Silicone)
L→R   **L**eft to **R**ight
L→L   **L**eft to **L**eft
R→L   **R**ight to **L**eft
R→R   **R**ight to **R**ight

1 Introduction

1.1 Historical Background

The phenomena regarding the seemingly completely random movement of small particles submerged in fluids puzzled physicists throughout the majority of 19th century. One of the first recorded studies of this motion was by Robert Brown in 1827. Brown was a biologist and botanist, and observed the seemingly chaotic movement by pollen particles submerged in water. Brown's first hypothesis was that the movement was pollen swimming, something akin to the swimming motion of sperm. This hypothesis was discarded as the same movement was observed by inorganic particles. Despite failing to explain the reason behind the motion, the phenomena was named Brownian motion after Brown.

Following Brown's study, physicists tried to establish a framework for describing the movement. This proved unsuccessful until 1905, when Albert Einstein (as Ph.D) published his paper "Investigations on the theory of Brownian Movement" [1]. The paper successfully provided a framework capable of explaining properties of the movement itself, and relate it to known fluid dynamics. Whilst not proven in Einstein's paper, he speculated that the forces causing the motion originate from the rapid movement of molecules. This hypothesis was later proven accurate.

In 1926 Jean Baptiste Perrin was awarded the Nobel prize in physics for his research which proved that matter consists of atoms. Perrin did so through a detailed study of Brownian motion, which connected the Brownian movement to the masses (and momentum) of individual atoms and molecules.

The laws established in Einstein's paper has been used frequently ever since. Today, apart from their obvious use in predicting diffusion rates and magnitudes, they play an important part in e.g the calibration of optical tweezers which are capable of confining nano- to microscale particles against forces of diffusion and other small scale forces. This allows detailed study of small scale systems, and are frequently used in studies of forces in small scale biology.

In the 19th century James Clerk Maxwell did substantial contributions to classical thermodynamics. One of his famous thought experiments is commonly referred to as Maxwell's demon. The demon was an attempt at a possible violation of the 2nd law of thermodynamics. It has powers which allows it to choose which particles which are allowed to do work, based on their kinetic energy. This in turn allows the demon to, if it so wishes, reduce the entropy in isolated systems without actually doing any work.

Such a violation has been proved to be impossible [2]. Still devices which are akin to Maxwell's demon are of interest in a range of science applications.

1.2 Relevance Today

Today there is ongoing research concerning Brownian motors. These devices rely on thermal fluctuations to generate a unidirectional net movement, and may in future applications serve as means of transport at the microscale. Their dependence on these fluctuations limits them to nanoscale devices. A current complication is a lacking framework for describing the thermal properties of such systems.

Stochastical thermodynamics [3] aims to couple the properties of non-equilibrium systems with those in equilibrium. To gain further understanding of such systems in

non-equilibrium, a study of the diffusion of particles in non-equilibrium is needed.

This thesis presents an important first step towards the creation of a feedback relay, which enables the study of particles in non-equilibrium. When thermal fluctuations drives a silica bead, of 1 µm diameter, up an inclined potential, the feedback raises barriers which prevents the bead from diffusing back to a lower potential. In this sense this device is akin to Maxwell's demon; the visual information of the bead's position is transformed into potential energy without actually doing any work on the bead. This allows detailed study of the bead in non-equilibrium.

The potential is an optical intensity gradient, as part of an optical line trap. The optical line trap is created by rapidly (2000 Hz) scanning a TEM_{00} laser in a line using an AOD (Acousto-optic deflector). The result is an approximately 20 µm long intensity gradient at focal length of a high numerical aperture objective.

This thesis begins with an introduction to the theory of Brownian motion in fluids, and another introduction to the active forces in an optical trap. The theory covered there is necessary to understand the remainder of the thesis. It is followed by section 3, where the method and experimental details of the experiment are presented. In section 4 obtained results are presented and discussed. Section 5 concludes the thesis with a conclusion and an outlook segment.

2 Theory

2.1 Brownian Motion

Microparticles suspended in a fluid undergo Brownian motion as a result of collisions with the molecules and atoms of the fluid. It manifests as a random motion of the particle. This movement cannot be predicted by other than statistical means, and further motion is independent of past motion.

The mean square displacement $\langle [\Delta x(t)]^2 \rangle$ and the related root mean square velocity $\bar{v}$, due to Brownian motion, in a single dimension during the time t is given by [4]

$$\langle [\Delta x(t)]^2 \rangle = 2Dt \tag{1}$$

$$\bar{v} = \frac{\sqrt{\langle [\Delta x(t)]^2 \rangle}}{t} = \sqrt{\frac{2D}{t}} \tag{2}$$

where D is the diffusion constant. The diffusion constant is given by[4]

$$D = \frac{k_B T}{\gamma} \tag{3}$$

where k_B is Boltzmann's constant, T is the temperature and γ is the Stokes frictional coefficient. The expression in Equation 3 is known as the Einstein relation and is one of the results presented in [1]. Stokes frictional coefficient is, for a perfect sphere, given by [4]

$$\gamma = 6\pi\eta r \tag{4}$$

where η is the viscosity of the medium and r the particles radius.

The position distribution of a diffusing particle in a single dimension follows the Boltzmann distribution. The probability of finding the system in the state i is [5]

$$p_i = \frac{e^{-E_i/k_B T}}{\sum\limits_{i=1}^{M} e^{-E_i/k_B T}} \tag{5}$$

where E_i is the energy of a state, k_B is Boltzmann's constant and T the temperature of the system. This leads to the following relation for the potential landscape U experienced by a diffusing particle at position x

$$U(x) = k_B T \ln\left(\frac{N(x)}{N(total)}\right) \tag{6}$$

where $N(x)$ is the counted occurrences at position x and $N(total)$ is the total number of tracked positions.

2.2 Optical Tweezers

Optical tweezers are useful for the study of small scale forces in the nano- to microscale. They rely on the resultant forces as the momentum of light changes as it is refracted by a particle. These forces are typically within the piconewton range and they scale with the intensity of the light. The trapping light originates from a laser. The laser wavelength can be chosen quite freely but infrared lasers are a common choice, in particular for applications involving the study of living organisms. Infrared light is then used as it has a low absorption rate in water, limiting damage dealt to the sample due to heating. The laser must however carry an intensity gradient for reasons that will soon become apparent.

A conventional optical tweezer traps particles in a point like region, which will be referred to as a point trap, but can be stretched into a line by rapidly scanning the laser beam in one dimension, which will be referred to as a line trap in this thesis.

Depending on the ratio between the diameter D of the particle and the wavelength λ of the light used for trapping, the models used for describing the interaction between the incoming light and a particle are different. If $D \gg \lambda$, the incoming light can be seen as collection of individual rays, for which the forces can be calculated separately. The net force would then be a vector sum from all contributing rays. This regime is sometimes referred to as the ray optics regime, or the geometric optics regime. If $D \ll \lambda$, the dielectric particle can be taken as a dipole in an electromagnetic field. This region is known as the Rayleigh regime. If $D \approx \lambda$ Mie scattering must be taken into account in the computation of forces, a nontrivial task which will not be dealt with here. For the application of these principles within this project, where $D \approx \lambda$, it is sufficient to understand that neither the ray optic regime nor the Rayleigh regime is entirely correct. Nonetheless, they provide a qualitative description.

For both regimes there are two important forces regarding optical tweezers; a gradient force and a scattering force. The gradient force functions as a restoring force. It pushes a particle back to an equilibrium point, against forces due to Brownian motion and those of the scattering force. The scattering force are due to light reflected (not refracted) from the particle and always carries a nonzero component along the propagation of light. A schematic of the gradient forces which traps the particle near the

focus can be seen in Figure 1(a) and (b). These schematics show the resulting force acting upon a trapped particle due to the refraction of rays of light.
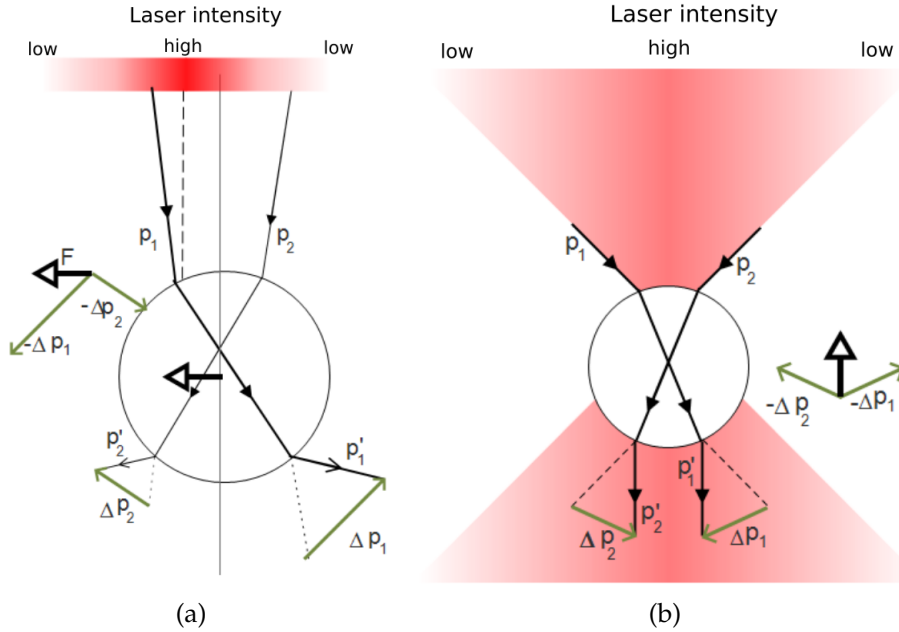

(a)   (b)

Figure 1: *The gradient force as result of the changed propagation of refracted light in the ray optics regime. Momentum changes $\Delta p_i = p_i - p_i'$ are considered and forces arise in the direction opposite to the change in momentum. In a) the principle which traps a particle in a plane perpendicular to the propagation of light. Rays with high intensity results in a larger change in momentum than rays of lower intensity. As a result the particle experiences a net force towards the propagation axis. In b) the principle which acts as a restoring force against the propagation of light for a particle positioned slightly beyond the focal point. The steep incident angle refracts rays so that the change of momentum pushes the particle opposite to the propagation of light. If the particle is positioned slightly before the focal point the net force would be pushing along the propagation of light.*

The origin of the scattering force in the Rayleigh regime is due to the resulting force along the propagation of light when photons are absorbed, and their isotropic re-emittance. This results in a non-zero net force along the propagation of light [6]

$$F_{scat} = n_m \frac{\sigma < S >}{c} \tag{7}$$

where c is the speed of light in vacuum, n_m is the refractive index of the medium, *<S>* is the time average of the Poynting vector and σ is the particle's cross section, which for a sphere in the Rayleigh regime is [6]

$$\sigma = \frac{8}{3} \pi k^4 r^6 \left(\frac{n_p^2 - 1}{n_p^2 + 2} \right)^2 \tag{8}$$

with particle radius r, k being the wavenumber of the light and n_p the refractive index of the particle.

Because the dielectric particle may be treated as a dipole in this regime ($D \ll \lambda$) there is an induced Lorenz force acting upon the particle in a electromagnetic field gradient.

This force always points towards a region of higher intensity [6]

$$\vec{F}_{grad}(\vec{z}) = n_m(2\epsilon_0 c)^{-1}\alpha\nabla I(\vec{z})^2 \tag{9}$$

where ϵ_0 is the vacuum permittivity, $I(\vec{z})$ is the laser intensity and α is the polarizability of the particle given by [6]

$$\alpha = \frac{n_m^2 r^3}{2}\left(\frac{n_p^2 - 1}{n_p^2 + 2}\right) \tag{10}$$

As the region of the highest intensity is at the focus of the objective the gradient force always pushes towards the focus, as well as towards the beam axis in general.

If D»λ, i.e the ray optics regime, the force due to a single ray of light being reflected by a dielectric and spherical particle can be derived by detailed ray tracing[3]. In this regime the scattering force arises from light reflected by the particle. The gradient force arises due to the beams refraction as it transits into, and out from, the medium and the particle. Just as in the Rayleigh regime the gradient force in the ray optics regime is always directed towards a region of higher intensity. In the ray optics regime the total force due to a single ray must also take into consideration the additional rays which are reflected within the sphere[3], as a consequence of a less than unity transmission coefficient at the surface. Hence the resulting force is an infinite sum, taking into consideration the Fresnel transmission and reflection coefficients, T and R. As a result the scattering force, G_{scat}, and the gradient force, G_{grad}, due to a single ray in the ray optics regime are [7]

$$G_{scat} = \frac{m_1 P}{c}\left(1 + R\cos 2\theta - \frac{T^2[\cos(2\theta - 2\Theta) + R\cos 2\theta]}{1 + R^2 + 2R\cos 2\Theta}\right) \tag{11}$$

$$G_{grad} = \frac{m_1 P}{c}\left(R\sin 2\theta - \frac{T^2[\sin(2\theta - 2\Theta) + R\sin 2\theta]}{1 + R^2 + 2R\cos 2\Theta}\right) \tag{12}$$

where $m_1 P/c$ is the incident momentum, θ is the angle of incidence and Θ is the angle of refraction.

Trapping occurs, in both regimes, when the gradient force dominates over the scattering force. For an unfocused beam the scattering force always dominate along the propagation of light, as the magnitude of the gradient force is then zero along the propagation. This is solved by using a highly focused laser beam. The rapid divergence of the light which occurs beyond the focal point results in a steep intensity gradient, with the gradient force directed opposite to the propagation of the beam.
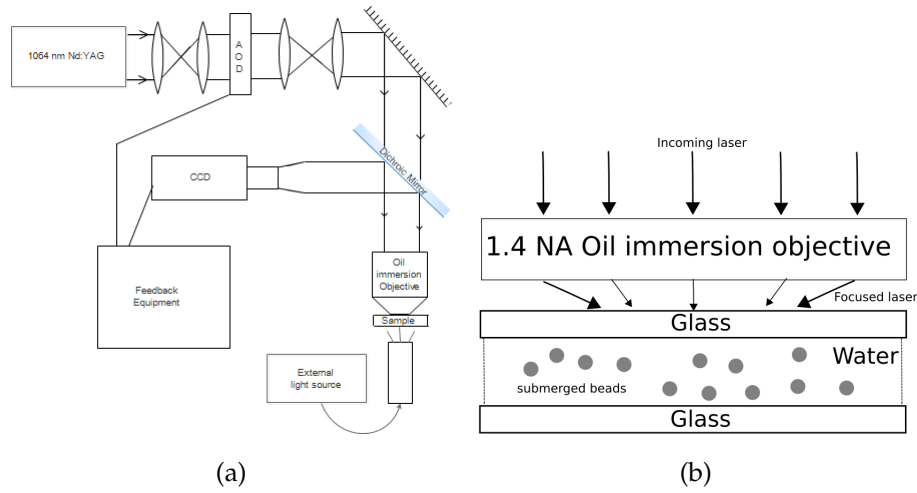
3 Experimental Details

Figure 2: *Schematic of the setup used for the trap, tracking and as well as that for implementing the barriers. In a) an overview schematic of all components in the setup. An AOD controls the intensity and deflection of an incoming 1064 nm laser, which is in turn focused by an oil immersion objective onto a sample. Bright-field images of the sample are captured by a CCD-camera, back lit by an external light source. In b) a close up schematic of the sample. The high NA objective focuses the TEM_{00} laser, allowing for trapping of a (or several) submerged silica bead.*

Silica beads with a diameter of 1 µm are mixed with diluted water and contained in a small chamber consisting of two glass surfaces, held together by a PDMS layer. The front glass surface is a 0.16 mm thick cover slip. A 1064 nm Nd:YAG laser (Spectra Physics, J20-BL10-1060) is focused onto the sample by an oil immersion objective (100x, NA 1.4, Leica Model, No. 11566014). By sweeping the laser in a line at 2000 Hz, an optical line trap (Figure 3) is generated. This is done using an acousto-optical deflector (AOD) controlled by one of two function generators.

The two function generators operate interchangeably with only one active at a time. Which function generator that is active is controlled by an electronic switch. Bright-field images of the sample are captured at 250 Hz using a CCD-camera and the positions of the beads are tracked using LabVIEW software. A schematic of the experimental setup and the sample is seen in Figure 2.

A histogram showing the result of a three minute tracking of the particle diffusion is shown in Figure 4(a). This data is then used to calculate the effective potential Figure 4(b) according to Equation 6.
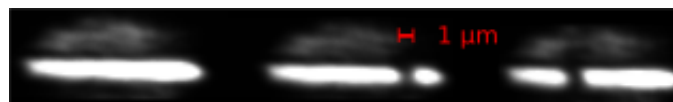

Figure 3: *Three images of an optical line trap created by rapidly scanning an optical tweezer in a line using an AOD. In two of the images there is a low intensity segment due to a fraction of the sweep with zero intensity output. This segment functions as a barrier, preventing trapped particles from crossing.*
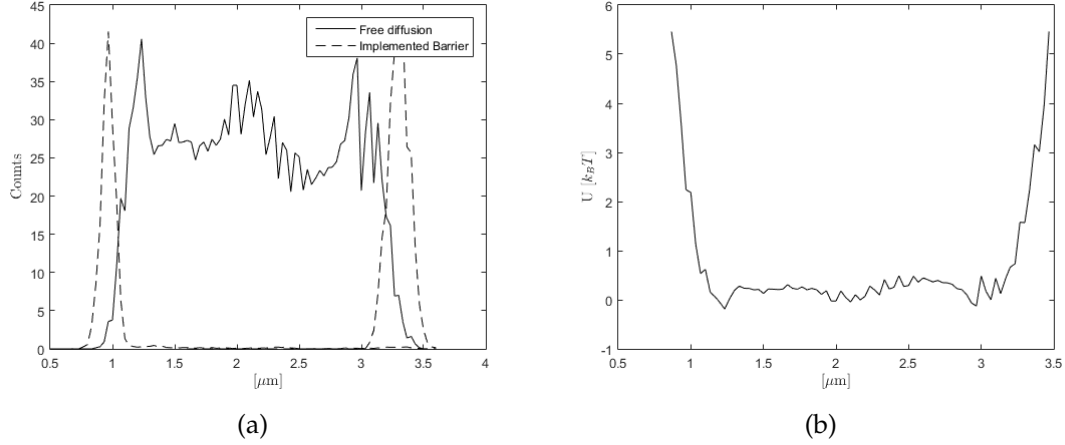
Figure 4: In a) the resulting histograms of the center position for a diffusion silica bead for three measurements are overlapped. One (solid line) where the bead diffuses freely and two (dashed lines) where a bead is confined to either side of a barrier. In b) the effective potential experienced by the freely diffusing particle in a).

3.1 Acousto-Optical Deflector

An AOD modulates the intensity and direction of a laser beam. It operates by sending acoustical waves, generated by a piezo crystal, through a Bragg crystal. The intensity and direction of a deflected beam depend on the properties of the crystal.

The acoustic wave alters the distance between layers within the crystal, which alters the refractive index and therefore the angle of the deflection. This angle θ depends on the acoustical frequency f as [8]

$$\Delta\theta = \frac{\lambda}{\Delta\Lambda} = \frac{\lambda\Delta f}{v} \tag{13}$$

where λ is the optical wavelength in the crystal, v is the velocity of the sound in the crystal and Λ is the distance between layers. The intensity I of the deflected beam depends on the radio frequency power P as [8]

$$\frac{I}{I_0} = \sin^2\left(\frac{\pi}{2}\sqrt{\frac{P}{P_0}}\right) \tag{14}$$

where I_0 is the initial laser intensity and P_0 is the optimal power for the specific AOD.

Equation 14 is, however, only valid at the optimal deflection angle, i.e the Bragg angle. This can be seen in Figure 5(b), where the output intensity of the AOD used in this project is shown as a function of deflection angle. The nonuniform output is inconsistent with Equation 14. In Figure 5(a) the output as a function of the radio frequency power at the Bragg angle is shown.

In this project the laser is swept rapidly in a line. As the laser spot size is finite there is an intensity overlay between a fraction of the sweep and fractions within a spot size radius around it. This has several consequences, such as that implemented barriers carry an intensity slope. This is also true for the trap edges. This concept is shown in Figure 6, where the intensity of the spot is approximated as flat rather than a Gaussian distribution.
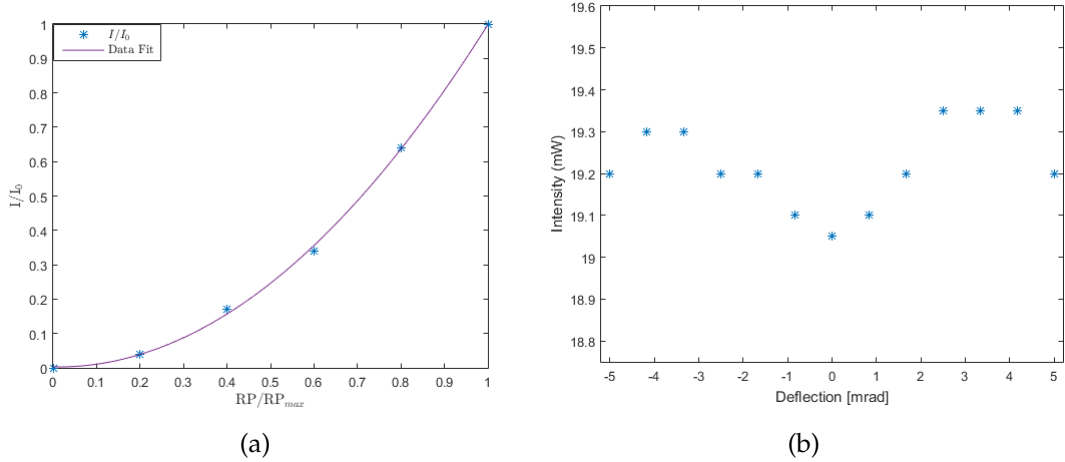
(a)   (b)

Figure 5: *In a) the measured output intensity of the deflected beam from the AOD as a function of the radio frequency power. Included is a line fit of the measured intensities. In b) the output intensity of the deflected beam from the AOD as a function of the deflection angle, in relation to the Bragg angle.*
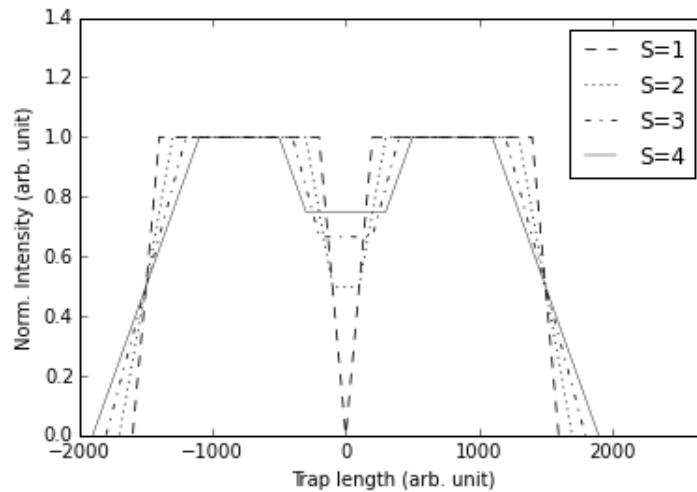

Figure 6: *The normalized intensity of a laser of uniform intensity swept in a line, with a fraction in the center where the output is zero. Despite this the fraction of the sweep will not have zero intensity, as the laser of any fraction leaks into neighboring fractions due to a finite beam spot size. The relative intensity for four different ratios, S, are shown, where S is the ratio between the beam spot size and the width of the zero output sweep fraction. The width of the zero output fraction is constant while the spot size is varied. A large value of S corresponds to a high relative intensity for the center fraction.*

When combined with the inaccuracy of equation 14 for higher deflected angles it complicates the scenario when adjustments are made to to the output wave function (which determines the output of the AOD), as changes made to a fraction of the sweep also affects an area around it. To account for this, when adjustments to the potential are needed they are made using an iterative process. This is done by measuring the effective potential, changing the radio frequency power for a fraction of sweep and measuring the new potential.

8

3.2 Method

The feedback algorithm developed is to implement a barrier in relation to a bead's position in the trap. This barrier is a region of low intensity and is generated with an AOD. Properties of these barriers are investigated in a series of measurements.

The barrier is implemented with the center of the bead and barrier aligning, and nearly aligning. The bead's velocity is measured before, and after the implementation of a barrier. Two separate barriers are used, one that is ≈0.34 μm wide, and one that is ≈0.46 μm wide. For each measurement the barrier is implemented when the center of the bead is tracked at a distance Δx from the center of the (to be) implemented barrier. This is done for Δx=[0, ±1/3, ± 1/6] μm.

The two cases whether the bead approaches the checkpoint from left or right are treated separately, and the x-axis is defined to be positive along the net propagation for both cases. This concept is shown and further explained in Figure 7. Furthermore the cases whether the bead ends up to the left or right of the barrier are also treated separately. As such there are in total 4 different cases.

For all parameters the bead is tracked until ≈190 000 data points are gathered.

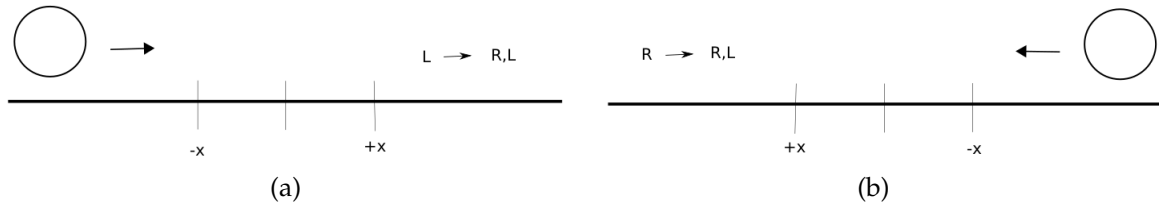***Figure 7:*** *Interpretation of the variable Δx throughout this thesis. The x-axis is defined as positive along the net propagation of the bead prior to feedback activation. As such the center of the bead has passed the center of the (to be) implemented barrier for $\Delta x > 0$ by a distance equal to Δx, irregardless whether the bead approaches from left (a) or right (b). Conversely the feedback is implemented prior passing the center of the (to be) implemented barrier by a distance of Δx for $\Delta x < 0$. If $\Delta x = 0$ the bead and barrier centers align at implementation time.*

4   Results and discussion

Results of measurements of the acceleration of a 1 µm silica bead, due to the intensity gradient of a barrier, are presented in this section. The results are presented in pairs, based on the sign of the variable Δx and the size of the implemented barrier.

Four cases are treated separately for each of these measurements. These cases depend on from which side of the trap the bead is prior to implementation, and at which side it ends up on after the barrier is implemented. As such there are four possible cases, two where the bead returns to the same side as before and two where it diffuses to the opposite side. These cases are denoted as L→L, L→R, R→L and R→R, where L is an abbreviation of left and R of right, with L and R directions as determined in Figure 4(a).

The trap was prior, and during, the experiment unstable in the sense that the bead fluctuates in and out of focus of the camera. This in turn lead to complications with tracking and feedback implementation. As a consequence a significant amount of data had to be discarded, and therefore it is probable that there are statistical errors and anomalies present in the results. This type of fluctuation was in particular prominent around the center of the trap, were there appeared to be a potential gradient which was difficult to climb for R→L,R cases. These cases spend a longer time around the center on average. Therefore these measurements had a higher ratio of discarded data. Due to this the data presented in $\Delta x = +1/6$ µm measurements had their R→R cases discarded in their entirety. The data in $\Delta x = +1/12$ µm cases also contain known errors but are displayed nonetheless as they may yet carry information regarding further, not yet identified, complications regarding the experiment.

High symmetry is observed in all figures between R→L and L→R cases with $\Delta x < 0$ µm, which is expected with the sweeping method utilized in this project. When the barrier size is mentioned it is important to remember that they carry an intensity gradient slope beyond the mentioned size. This slope extends beyond the mentioned size plus the spot size of the laser. The bead experiences the gradient as long as it still remains in the gradient, as such the radius of the bead must clearly be taken into account when interpreting the results. The figures in this section track the center of the bead, and therefore the plots should be shifted by 0.5 µm (the bead radius) when the radius must be considered.
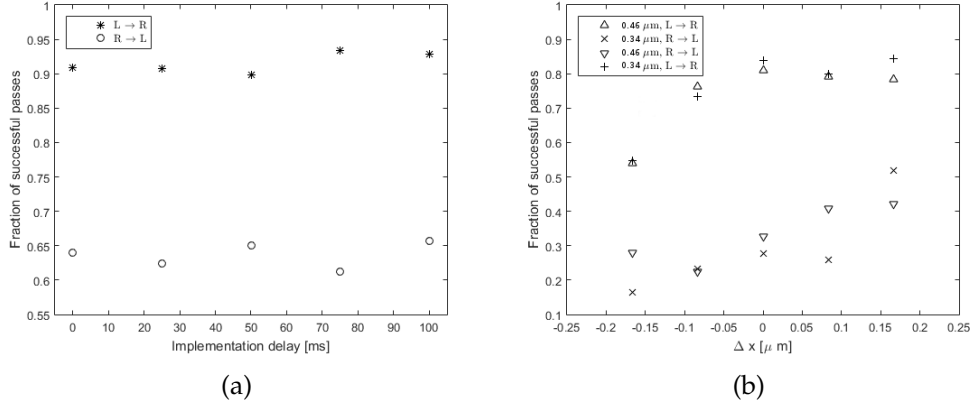
(a)   (b)

Figure 8: *The fraction of times a bead diffuses past a checkpoint and ends up on the opposite side after the implementation of a barrier. In a) as a function of displacement from the implementation point for barriers of different size. Δx is defined so that x is positive along the propagation of the bead. In b) as a function of an implementation delay with $\Delta x = 0$, i.e the time the bead diffuses after reaching the implementation point before the barrier is implemented. This delay is in addition to any inherent delay of the setup.*

Observing Figure 8 it becomes clear that there is a lack of symmetry in the experiment. The probability for a successful pass is far higher for L→R than R→L. This holds true for both barriers. The reason for this becomes clear when these cases are compared in any combination of figures in this section. The initial velocity prior to implementation is far higher for L→R than for R→L,R, resulting in a higher passing rate for L→R. The reason for the high initial velocity for L→R originates from that the barrier was not situated exactly in the middle of the trap, but slightly to the left. This can be seen in Figure 4(a). Prior to the release of the barrier beads pushed to the left are kept in a higher potential than beads pushed to the right. The bead's velocity in the L→R cases did not have time to dissipate prior implementation. The resulting lack of symmetry renders any further comparison between L→R and R→L,R cases redundant.
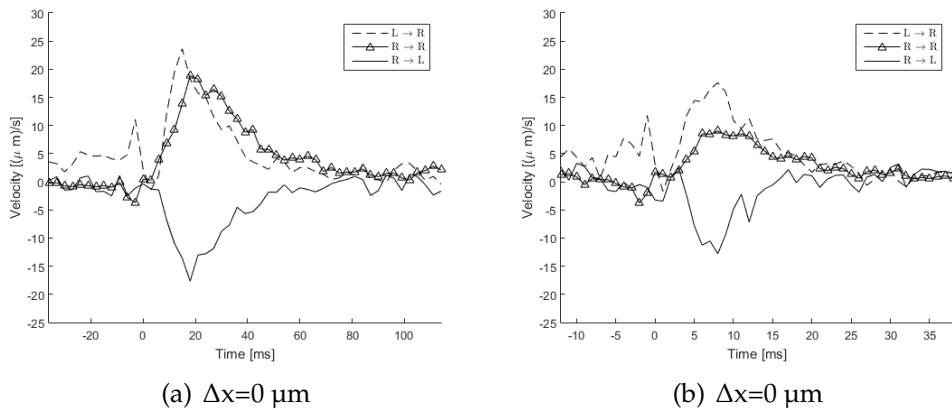

(a) $\Delta x = 0$ μm   (b) $\Delta x = 0$ μm

Figure 9: *The velocity of a 1 μm silica bead after being pushed by a barrier of width ≈0.34 μm (a) and ≈0.46 μm (b) implemented at t=0. The changed variable Δx is the distance between the center of the bead and the center of the (to be) implemented barrier at t=0, with a positive x-axis along the net propagation of the bead prior to implementation.*
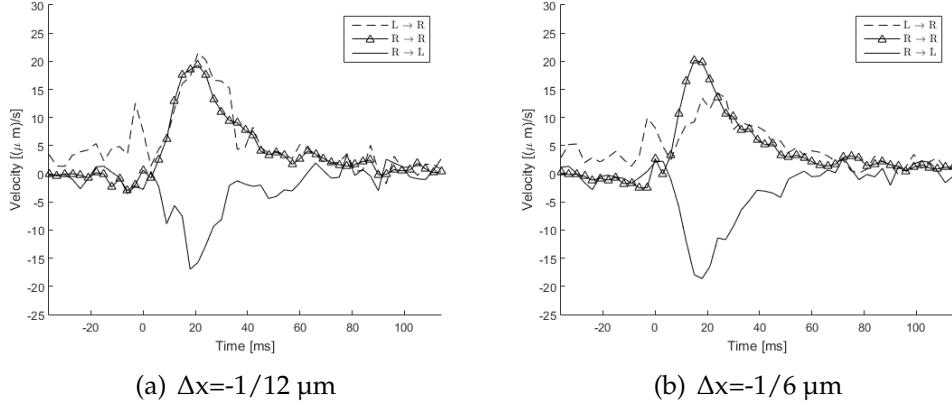
11

(a) Δx=-1/12 µm

(b) Δx=-1/6 µm

Figure 10: *The velocity of a 1 µm silica bead after being pushed by a barrier of width ≈0.34 µm implemented at t=0. The changed variable Δx is the distance between the center of the bead and the center of the (to be) implemented barrier at t=0, with a positive x-axis along the net propagation of the bead prior to implementation.*

The R→L and R→R cases are highly symmetric for Δx < 0, which implies that the barrier itself is symmetric. There are however discrepancies which differ the two cases.

There are bumps in the R→L cases, which are seen in all measurements at approximately the same distance traveled after t=0. As it occurs so frequently, and similar behavior for all measurements, are these unlikely to merely be statistical anomalies. Rather, they are remnants of the iterative process used when creating the trap potential. An intensity change in a small fraction of the trap also affects the intensity in a laser spot size radius around it. As such there is no reason to assume that just because the potential is uniform that the intensity output by each fraction of the sweep is. Instead it is merely the sum of the intensity output in the nearby fraction which end up (nearly) uniform. The observed bumps are then due to that the fraction of the sweep which leaks onto the barrier slope is not uniform, with intensity gradient "speed bumps" as a result.
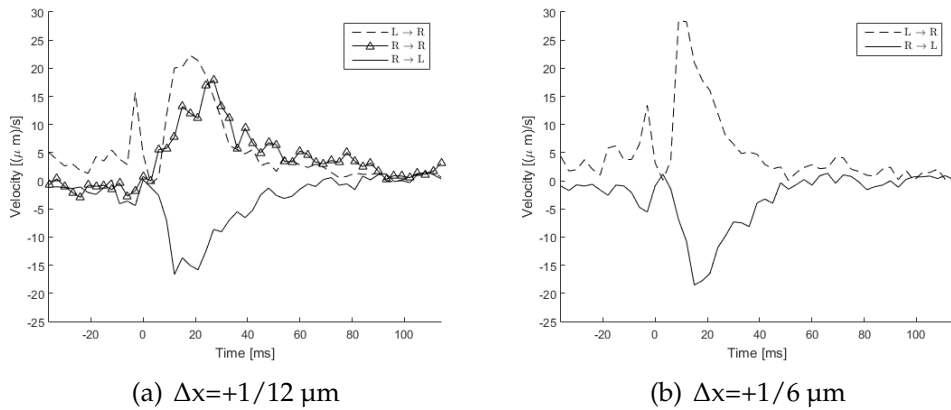

(a) Δx=+1/12 µm

(b) Δx=+1/6 µm

Figure 11: *The velocity of a 1 µm silica bead after being pushed by a barrier of width ≈0.34 µm implemented at t=0. The changed variable Δx is the distance between the center of the bead and the center of the (to be) implemented barrier at t=0, with a positive x-axis along the net propagation of the bead prior to implementation.*

12

(a) Δx=-1/6 μm   (b) Δx=-1/12 μm

Figure 12: *The velocity of a 1 μm silica bead after being pushed by a barrier of width ≈0.46 μm implemented at t=0. The changed variable Δx is the distance between the center of the bead and the center of the (to be) implemented barrier at t=0, with a positive x-axis along the net propagation of the bead prior to implementation.*
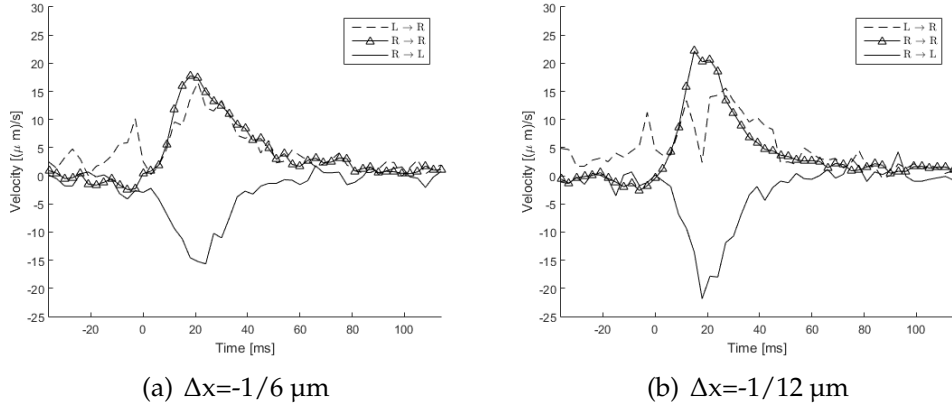
A surprising result is that the resulting velocities from the 2 barriers has equal magnitude, even more so with highly similar accelerations. The larger barrier was expected to generate slightly larger velocities, with a stronger initial acceleration due to a steeper intensity gradient. This hypothesis was largely based with a spot size to barrier width ratio of approximately unity for the larger barrier in mind. As is seen in figure 6 the relative intensity, between barrier region and flat regions of the trap, depends on this ratio. It is possible that the expected results could not be observed at the given resolution, due to a too large spot size to barrier width ratio. Further measurements with a larger range of barrier sizes could provide clarity in the matter, without any further requirements on resolution.
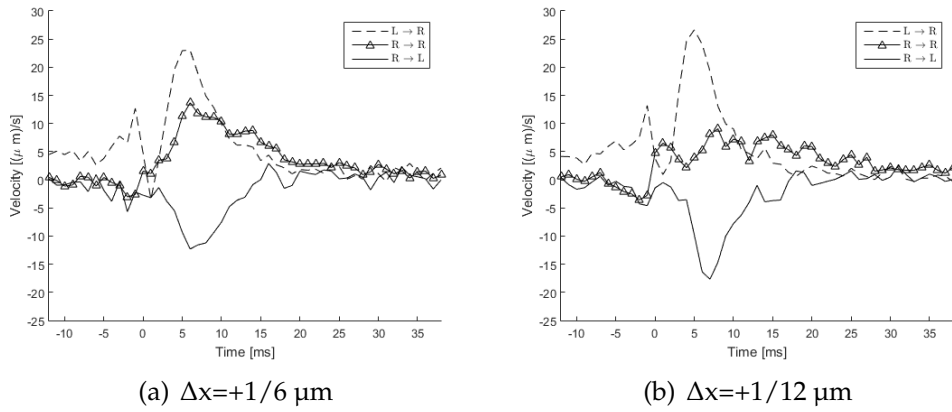

(a) Δx=+1/6 μm   (b) Δx=+1/12 μm

Figure 13: *The velocity of a 1 μm silica bead after being pushed by a barrier of width ≈0.46 μm implemented at t=0. The changed variable Δx is the distance between the center of the bead and the center of the (to be) implemented barrier at t=0, with a positive x-axis along the net propagation of the bead prior to implementation.*

13

The gradient becomes stabilized at a distance from the edge of the barrier equal to half the spot size radius of the beam. Still relying on the approximated spot size of 0.5 μm this entails that this range is 0.25 μm outside the barriers edges. The distance covered for the negative Δx cases before rapid deceleration occurs is ≈ 0.4 μm. This positions the center of the bead well beyond the stabilization point, with a weaker gradient force as a result. The gradient force still acts upon the bead, but the force decreases beyond this point. This, along with the drag force, marks the beginning of the deceleration process.

Concerning the L→R cases there is a sharp velocity peak just before t=0. No explanation for this peak has been found, but it is not expected to be a real entity despite its high prevalence. It could be an artifact from the feedback and tracking processes, albeit it is not confirmed. This suspicion arises as it the peak is situated within 3 ms of t=0. With a frame rate of 250 Hz there should be no data points within this window. Naturally there are fluctuations to the frame rate, as such there will on occasion end up data points within this time window. However, in the raw data there were several data points within 1 ms of each other, even those separated by 0 ms (rounded off, this was the current limit of time resolution). This should be considered a highly unlikely occurrence, an erroneous behavior even. It is likely a problem either with the computers measurement of time, e.g sporadic freezes, or with some part of the feedback code. This shows that there are still improvements which could be made to the feedback in this project.

The significantly lower velocities reached for the $\Delta x = 0$ and $\Delta x = 1/12$ μm, R→R, cases are due to remnants of erroneous data which were not possible to remove. These remnants are low in number but do still exist in all velocity plots but heavily effects the outcome in Figure 9(b) and Figure 13.

5   Conclusions and Outlook

Insufficient data entails that all presented results likely include statistical fluctuations and anomalies. As the reason for the discarding of measurement data originates from an unsuccessfully calibrated trap, and that the reason for this mainly lies in the taxing, manual, iterative method utilized, the best improvement for further experiments using a similar setup may be to improve the calibration method.

To reduce the amount of work needed for calibration there are two suitable paths to take. First off; a lot of the calibration work could be automated using computer software. Full automation is however only recommended if the sample can be moved by electrical motors. The reason for this is the bead's proneness to escape an uncalibrated line trap. Without any mechanism to chase the bead and bringing it back to the original position the automated process would be very time consuming. The process must then rely on another bead diffusing into the trap, without any guarantee that the new bead experiences the same potential as the first. Even small differences in shape or size of the beads can have significant effects on the effective potential. It would also be possible to do a semi-automatic approach.

The second method, which is highly recommended, would be to make full range investigation of the output of the AOD at a range of frequency and radio frequency power inputs, i.e a more in depth investigation along the lines of the one presented in figure 5(b). This would be a straightforward way of mapping the output of a given fraction of the sweep, likely bypassing a lot of the iterative work. In addition this data could always be used for any troubleshooting of the AOD and related components.

This project would have benefited from a longer trap. A longer trap would have allowed for a wider range of barrier widths to be tested, as well as for larger values of Δx. In the presented results there were no clear differences between the resulting velocities of the two barriers, perhaps due to too small differences in laser spot size to barrier ratios. Perhaps this could be confirmed in a longer trap, with larger implemented barriers.

Larger values of Δx could test for the extent of the barrier's slope. Knowledge of the extent of this slope is useful for the next stage of the developed feedback, involving the mimicking of Maxwell's demon. For that application no pushing of the bead at the implementation of the barrier should occur. To ensure that this does not happen, larger values of Δx can find the regime where pushing no longer occurs, i.e an experimental confirmation of the full extent of the barriers.

The presented data allows for an experimental determination of the gradient force acting upon the bead in the presence of the barriers. Only two forces act upon the bead in the observed timespan. Those are the gradient force, which is the driving force, and the drag force, which is proportional to the bead's velocity. As the drag force is well defined given the parameters of this experiment, the gradient force can be computed from the presented data. This in turn could be compared to theoretical calculations which take Mie scattering into consideration, providing an alternative way to map the intensity of trap segments.

References

[1] Einstein A. Investigations on the theory of brownian movement. *New York: Dover*, 75, 1956. (Translation of orginal publication from 1905).

[2] Harvey S. L. *Maxwell's demon 2 : entropy, classical and quantum information, computing*. Institute of Physics, 2003.

[3] Seifert U. Stochastic thermodynamics, fluctuation theorems and molecular machines. *Rep. Prog. Phys.*, 75, 2012.

[4] Tongcang L. Measurement of the instantaneous velocity of a brownian particle. *Science*, 328, 2010.

[5] Pathria P. K. *Statistical Mechanics 3rd ed.* Elsevier Science, 2011.

[6] Ashkin A. Acceleration and trapping of particles by radiation pressure. *Physical review letters*, 24(4), 1970.

[7] Ashkin A. Forces of a single-beam gradient laser trap on a dielectric sphere in the ray optics regime. *Biophysical Journal*, 61, 1992.

[8] Hosaka S. High speed laser beam scanning using an acousto-optical deflector. *Japanese Journal of Applied Physics*, 26, 1987.